Commun. Comput. Phys.
doi: 10.4208/cicp.OA-2023-0295

Vol. **36**, No. 1, pp. 104-132
July 2024

Modeling Two-Phase System in Complex Domains Based on Phase-Field Approach with Interfacial Correction

Jingwen Wu[1] and Zhijun Tan[1,2,*]

[1] *School of Computer Science and Engineering, Sun Yat-sen University, Guangzhou 510006, China.*
[2] *Guangdong Province Key Laboratory of Computational Science, Sun Yat-sen University, Guangzhou 510006, China.*

Received 14 November 2023; Accepted (in revised version) 24 April 2024

Abstract. We introduce a novel phase-field model designed for ternary Cahn-Hilliard (CH) dynamics, incorporating contact angle boundary conditions within complex domains. In this model, we utilize a fixed phase field variable to accurately represent intricate domains within the ternary CH system. Simultaneously, the remaining two phase field variables are employed to simulate CH dynamics effectively. The contact angle term is derived from Young's equality and the hyperbolic tangent profile of the equilibrium interface. To ensure compliance with the hyperbolic tangent property at the interface, a fidelity term is incorporated into the original CH model. This addition reduces mass loss for each phase and improves the accuracy of the contact angle effect. Moreover, we implement a finite difference scheme along with a nonlinear multigrid method to solve the corrected ternary CH model. A series of numerical experiments is conducted in both two- and three-dimensional spaces to demonstrate the efficiency and robustness of the proposed model.

AMS subject classifications: 35K55, 35J60, 65M06

Key words: Ternary Cahn–Hilliard system, complex domains, hyperbolic tangent property, multigrid method.

1 Introduction

The Cahn-Hilliard (CH) equation, originally formulated by Cahn and Hilliard [1], represents a fundamental phase-field model utilized to describe the mass-conserved spinodal

*Corresponding author. *Email addresses:* wujw87@mail2.sysu.edu.cn (J. Wu), tzhij@mail.sysu.edu.cn (Z. Tan)

 ©2024 Global-Science Press

decomposition observed in binary alloys. In the CH equation, an order parameter, referred to as the phase-field variable, is introduced to characterize the physical state of the system. Notably, this phase-field variable assumes distinct values within each phase, with, for instance, -1 representing the liquid phase and 1 representing the solid phase. The interface separating these phases is characterized by a continuous and finite transition layer, and its position can be defined as a level set of the phase-field function. This unique formulation allows implicit capture of topological changes in the interface during the solution process. Moreover, it is worth noting that the CH equation naturally satisfies mass conservation when either periodic or homogeneous Neumann boundary conditions are applied. The CH equation, governing the behavior of the phase-field variable, adheres to the H^{-1}-gradient flow principle of the total free energy. Through appropriate modifications, the original CH equation has found wide-ranging applications in modeling diverse physical phenomena, including but not limited to diblock copolymer dynamics [2–4], surfactant behavior [5–7], contact angle and wetting phenomena [8, 9], the dynamics of gravity and capillary waves [10], solid tumor growth [11, 12], as well as applications in topology optimization and image processing [13, 14], etc..

Many real-world physical phenomena and natural processes, such as the formation of double emulsions in micro-fluidic devices [15, 16], the behavior of hydrocarbon fluids in the petroleum industry [17], the intricate dynamics of water-oil-surfactant mixtures [18, 19], and multi-component chemo-mechanics [20], etc., inherently involve more than two components, including substances like water, surfactants, alcohols, and other immiscible materials. Researchers, such as Fontaine [21] and Morral and Cahn [22], have extended the CH model to address multi-component systems, enabling the modeling of the dynamic behavior of materials featuring multiple phases within their microstructures. In the multi-component CH phase-field model, tailored for systems involving more than two components, a minimum of three phase-field variables is employed, with each variable representing an individual component. For instance, a value of 1 signifies the presence of the respective component, while 0 indicates its absence. This multi-component CH model has found widespread application in fluid simulations. For instance, Kim [23] introduced a generalized continuous surface tension force model to account for surface tension effects in multi-component fluid flow. Lee and Kim [24] conducted a numerical investigation into buoyancy-driven mixing of incompressible immiscible fluids, involving multi-component CH equations, within two-dimensional tilted channels. Additionally, Zhang et al. [25] delved into the ramifications of droplet inertia and interfaces, utilizing an incompressible fluid flow-coupled ternary CH model to analyze the flow dynamics during the collision of two immiscible droplets. This allowed them to evaluate factors such as film thickness, maximal spreading time, and deformation, with a particular focus on the liquid-liquid interface. Furthermore, Kalantarpour et al. [26] constructed a ternary phase-field Lattice Boltzmann model to explore scenarios involving high-density ratios and total spreading within three incompressible and immiscible fluids. Their work showcased the utilization of multi-component CH equations to monitor the phasic evolution of the system. The simulation results in the context

of bubble-droplet interactions illuminated that off-center collisions yielded higher film drainage and coalescence times compared to head-on impacts.

Numerous multiphase flow phenomena manifest not only within regular domains, such as 2D rectangular or 3D cuboid configurations but also in intricately irregular, complex domains. Researchers have devised various approaches to address these complexities. Li et al. [27] introduced a direct discretization method for solving multi-component CH systems on surfaces employing surface meshes comprising piecewise triangles and their dual-surface polygonal tessellations. Xia et al. [28] devised an innovative surface discrete finite volume method to address binary fluid flow models on arbitrarily curved surfaces. In contrast, Tan et al. [29] adopted a different approach, simulating multiphase fluids within 3D narrow band domains, encompassing the surfaces. For an extensive array of methods concerning arbitrarily curved surfaces, we refer readers to [30–33] and the associated references. Jeong et al. [34] introduced a modified ternary CH system within a complex domain, employing a phase-field variable to define the arbitrary domain. Notably, the phase-field variable remained fixed during the temporal evolution of the other two phases. Validation of the modified CH system's performance was achieved through simulations in both 2D and 3D complex domains. The influence of the contact angle [35–37] between the fluid and solid is pivotal in wetting or non-wetting simulations. Taking into account contact angle boundary conditions and the fixed phase condition within complex domains, Li et al. [38] proposed an efficient phase-field model for multi-component CH systems, accommodating various boundary conditions in complex domains. By coupling the modified ternary CH equation with the NS equation, Yang and Kim [39] simulated two-phase flows in arbitrary domains while considering the effects of contact angles. In the paper [40], Yang et al. detailed the estimation of energy stability for the modified ternary CH equation within arbitrary domains and employed the scalar auxiliary variable approach for its solution.

In previous models, the incorporation of the contact angle condition into the chemical potential within the CH system relied on the utilization of a hyperbolic tangent profile for the equilibrium interface at boundaries. This approach aimed to satisfy the surface energy formulation, as established by Young's equation [41]. However, the inherent dynamics of interface length minimization in the CH equation did not consistently ensure that the interface transitions between different phases followed hyperbolic tangent profiles. To address this issue and minimize the interface length minimization property, Li et al. [42] introduced a corrective term for the interfacial profile within the original CH equation. This corrective term serves to enforce a hyperbolic tangent profile for the phase-field profile. Building upon this development, Xia et al. [43] extended the interfacial profile correction term to encompass the multi-component immiscible flows model.

This study aims to propose an corrected ternary CH model incorporating contact angle boundary conditions within complex domains. The inherent dynamics of the original ternary CH model present a challenge, as they do not inherently yield hyperbolic transitions between multiple phases, a crucial consideration for accurate representation of contact angle conditions. To rectify this, an interfacial profile correction term will be

introduced into the original ternary CH model. This corrective measure effectively enforces a hyperbolic tangent profile for the phase-field, thereby mitigating mass loss in each phase. The computational solution of the corrected ternary CH equation will be facilitated through the application of an efficient multigrid method, grounded in the finite difference technique. The paper includes several numerical examples in both 2D and 3D domains, serving to illustrate the effectiveness and precision of the proposed model. Comparative analyses with the original ternary CH model, conducted through numerical tests, underscore the model's capability to maintain the hyperbolic tangent property while concurrently reducing mass loss in each phase.

The remainder of this paper is organized as follows. An corrected phase-field model for a ternary CH system in a complex domain is formulated in Section 2. In Section 3, numerical scheme is given. Various numerical examples are carried out in Section 4. Finally, the paper is concluded in Section 5.

2 Governing equations

Let us consider a ternary CH system within a domain $\Omega \subset \mathbb{R}^{dim}$, where $dim=2$ or $dim=3$. Ω_{in} is a complex subdomain within Ω, as illustrated in Fig. 1(a).

Each component of the ternary mixture is represented by a function $\phi_k(\mathbf{x},t)$ defined across space $\mathbf{x}$ and time t, referred to as the order parameter. This order parameter signifies the mole fraction of the respective component in the mixture, i.e.,

$$\phi_k = \begin{cases} 1, & \text{inside the } k\text{-th phase,} \\ 0, & \text{outside the } k\text{-th phase,} \quad k=1,2,3. \end{cases} \tag{2.1}$$

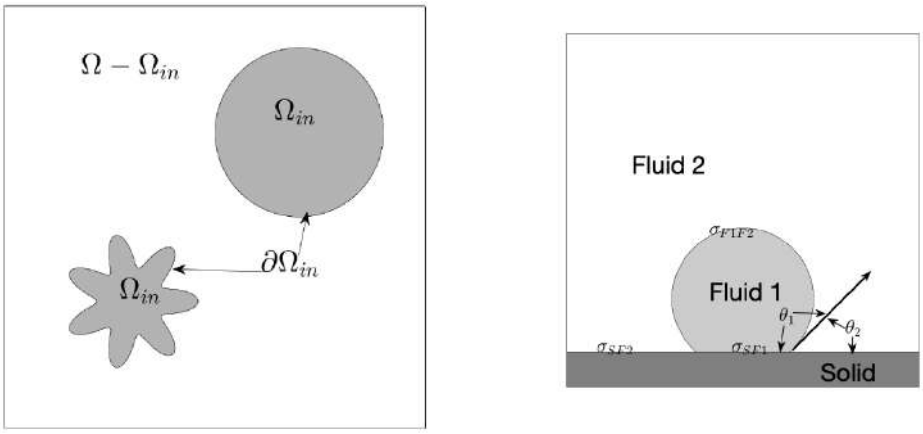

(a) (b)

Figure 1: Schematic illustrations of (a) complex regions and (b) contact angle among three phases.

In accordance with the principle of mass conservation, the summation of mole fractions adheres to the following equation

$$\phi_1(\mathbf{x},t)+\phi_2(\mathbf{x},t)+\phi_3(\mathbf{x})=1. \tag{2.2}$$

We employ a fixed phase variable $\phi_3(\mathbf{x},\mathbf{t})$ to characterize the arbitrary domain Ω_{in}, i.e.,

$$\phi_3(\mathbf{x},t)=\begin{cases}1, & \text{if } \mathbf{x}\in\Omega_{in},\\ 0, & \text{if } \mathbf{x}\in\Omega-\Omega_{in}.\end{cases} \tag{2.3}$$

The boundary of the arbitrary domain Ω_{in} is the 0.5-level set of ϕ_3. The determination of the contact angle between fluid and solid surfaces is crucial for simulating wetting and non-wetting phenomena. In this context, our focus lies specifically on the dihedral contact angle occurring at the interface among the three distinct components, as illustrated in Fig. 1(b). Here, Fluid 1 is denoted by ϕ_1 while Fluid 2 is represented by ϕ_2. The contact angles for ϕ_1 and ϕ_2 are labeled as θ_1 and θ_2, respectively, and they are complementary angles.

The ternary model describing the CH dynamics with different contact angle conditions in arbitrary domain can be derived from the following energy functional

$$\begin{aligned}\mathcal{E}_{CHmod}(\phi)&=\sum_{k=1}^{2}\mathcal{E}_{CHmod_k}(\phi)\\ &=\sum_{k=1}^{2}\int_{\Omega}\left(F(\phi_k)+\frac{\epsilon^2}{2}(1-\phi_3)|\nabla\phi_k|^2+\underbrace{\epsilon\left(\frac{1}{3}\phi_k^3-\frac{1}{2}\phi_k^2\right)|\nabla\phi_3|\cos\theta_k/\sqrt{2}}_{I}\right)d\mathbf{x},\end{aligned} \tag{2.4}$$

where $F(\phi_k)=0.25\phi_k^2(\phi_k-1)^2$ is the homogenous free energy, ϵ represents a small positive constant associated with the thickness of the diffuse interface separating two components. The nonlinear term I is the contact angle term, by which we can investigate different contact angle conditions. It is established upon a hyperbolic tangent profile that characterizes the equilibrium interface at the boundaries, incorporating Young's equality. Note this kind of energy functional has been extensively used for various ternary physical systems [38–40, 44, 45].

The original CH equation possesses inherent dynamics, specifically the minimization of interface length through motion. The resulting interfacial transitions between different phases deviate from hyperbolic tangent profiles, which holds significance for establishing the contact angle condition and leads to the nonconservation of the enclosed area. To

address this shortcoming, we add a fidelity term into Eq. (2.4), i.e.,

$$\begin{aligned}\mathcal{E}_{corrected}(\phi) &= \mathcal{E}_{CHmod}(\phi)+\mathcal{E}_F(\phi)\\ &=\sum_{k=1}^{2}\mathcal{E}_{CHmod_k}(\phi)+\sum_{k=1}^{2}\mathcal{E}_{F_k}(\phi)\\ &=\sum_{k=1}^{2}\int_\Omega\left(F(\phi_k)+\frac{\epsilon^2}{2}(1-\phi_3)|\nabla\phi_k|^2+\epsilon\left(\frac{1}{3}\phi_k^3-\frac{1}{2}\phi_k^2\right)|\nabla\phi_3|\cos\theta_k/\sqrt{2}\right)d\mathbf{x}\\ &\quad+\sum_{k=1}^{2}\int_\Omega\frac{\lambda}{2}(1-\phi_3)\left(\frac{\phi_k(1-\phi_k)}{\sqrt{2}\epsilon}-|\nabla\phi_k|\right)^2 d\mathbf{x},\end{aligned}\tag{2.5}$$

where $\lambda>0$ is a constant. When the phase-field across the interface is a hyperbolic tangent profile we have

$$|\nabla\phi_k|=\phi_k(1-\phi_k)/(\sqrt{2}\epsilon),\tag{2.6}$$

which is derived from $F(\phi_k)=\frac{\phi_k^2(\phi_k-1)^2}{4}=\frac{\epsilon^2}{2}|\nabla\phi_k|^2$, see Xia et al. [43] and the references therein. Minimizing $\mathcal{E}_F(\phi)$ forces the phase-field profile to be a hyperbolic tangent profile. Therefore, the modified version of total energy, Eq. (2.5), has the capacity to induce a hyperbolic tangent profile for the interface between the two phases.

By taking the variational approach to Eq. (2.5) with respect to ϕ, the corrected ternary CH equation can be derived by a 'gradient flow' a [43]

$$\frac{\partial\phi_k}{\partial t}=M\nabla\cdot((1-\phi_3)\nabla\mu_k)-\lambda M\frac{\delta\mathcal{E}_{F_k}}{\delta\phi_k},\tag{2.7}$$

$$\mu_k=\frac{\delta\mathcal{E}_{CHmod_k}}{\delta\phi_k}+\beta(\Phi),\quad k=1,2,\tag{2.8}$$

where μ_k is the kth chemical potential and $M>0$ is a constant mobility. We take $M\equiv1$ for convenience. To ensure the constraint in Eq. (2.2), a Lagrange multiplier $\beta(\Phi)$ [46] is imposed on the chemical potential. The periodic boundary condition or the following zero-Neumann boundary condition, i.e.,

$$\nabla\phi_k\cdot\mathbf{n}|_{\partial\Omega}=\nabla\mu_k\cdot\mathbf{n}|_{\partial\Omega}=0,\quad \text{for } k=1,2,\tag{2.9}$$

is used on all boundaries of domain Ω.

The variational derivatives of $\mathcal{E}_{F_k}$ and $\mathcal{E}_{CHmod_k}$ with respect to ϕ_k are given as

$$\frac{\delta\mathcal{E}_{CHmod_k}}{\delta\phi_k}=f(\phi_k)-\epsilon^2\nabla\cdot((1-\phi_3)\nabla\phi_k)+\epsilon\phi_k(\phi_k-1)|\nabla\phi_3|\cos\theta_k/\sqrt{2},\tag{2.10}$$

$$\begin{aligned}\frac{\delta\mathcal{E}_{F_k}}{\delta\phi_k}=\lambda\Bigg((1-\phi_3)\frac{\phi_k(\sqrt{2}\epsilon|\nabla\phi_k|-\phi_k(1-\phi_k))}{\epsilon^2}-\nabla\cdot((1-\phi_3)\nabla\phi_k)\\ +\frac{1}{\sqrt{2}\epsilon}\nabla\cdot\left((1-\phi_3)(1-\phi_k)\phi_k\frac{\nabla\phi_k}{|\nabla\phi_k|}\right)\Bigg),\end{aligned}\tag{2.11}$$

where $f(\phi_k)=F'(\phi_k)=\phi_k(\phi_k-1)(\phi_k-0.5)$. Because we have

$$\begin{aligned}
&\frac{d}{d\xi}\mathcal{E}_{CHmod_k}(\phi_k+\xi\psi)|_{\xi=0}\\
&=\int_\Omega(\psi F'(\phi_k)+(1-\phi_3)\epsilon^2\nabla\psi\cdot\phi_k)\,d\mathbf{x}\\
&\quad+\int_\Omega\psi\epsilon\phi_k(\phi_k-1)|\nabla\phi_3|\cos\theta_k/\sqrt{2}\,d\mathbf{x}\\
&=\int_\Omega(F'(\phi_k)-(1-\phi_3)\epsilon^2\Delta\phi_k)\psi\,d\mathbf{x}+(1-\phi_3)\int_{\partial\Omega}\epsilon^2\frac{\partial\phi_k}{\partial\mathbf{n}}\psi\,ds\\
&\quad+\int_\Omega\psi\epsilon\phi_k(\phi_k-1)|\nabla\phi_3|\cos\theta_k/\sqrt{2}\,d\mathbf{x}\\
&=\int_\Omega(F'(\phi_k)-\epsilon^2\nabla\cdot((1-\phi_3)\nabla\phi_k)+\epsilon\phi_k(\phi_k-1)|\nabla\phi_3|\cos\theta_k/\sqrt{2})\psi\,d\mathbf{x}, \qquad (2.12)\\
&\frac{d}{d\xi}\mathcal{E}_{F_k}(\phi_k+\xi\psi)|_{\xi=0}\\
&=\lambda\int_\Omega\left((1-\phi_3)\frac{\phi_k(\sqrt{2}\epsilon|\nabla\phi_k|-\phi_k(1-\phi_k))}{\epsilon^2}-\nabla\cdot((1-\phi_3)\nabla\phi_k)\right.\\
&\quad\left.+\frac{1}{\sqrt{2\epsilon}}\nabla\cdot\left((1-\phi_3)(1-\phi_k)\phi_k\frac{\nabla\phi_k}{|\nabla\phi_k|}\right)\right)\psi\,d\mathbf{x}. \qquad (2.13)
\end{aligned}$$

Here, $\int_\Omega\psi\,d\mathbf{x}=0$ and $\partial\phi_k/\partial\mathbf{n}=0$ at $\partial\Omega$ are used. $\mathbf{n}$ represents the unit outward normal vector to the boundary $\partial\Omega$.

The governing equations of the corrected ternary CH system can be represented by

$$\begin{aligned}
\frac{\partial\phi_k}{\partial t}&=M\nabla\cdot((1-\phi_3)\nabla\mu_k)-\lambda M\left((1-\phi_3)\frac{\phi_k(\sqrt{2}\epsilon|\nabla\phi_k|-\phi_k(\phi_k-1))}{\epsilon^2}\right)\\
&\quad+\lambda M\left(\nabla\cdot((1-\phi_3)\nabla\phi_k)-\frac{1}{\sqrt{2\epsilon}}\nabla\cdot\left((1-\phi_3)(1-\phi_k)\phi_k\frac{\nabla\phi_k}{|\nabla\phi_k|}\right)\right), \qquad (2.14)\\
\mu_k&=f(\phi_k)+\beta(\Phi)+\epsilon\phi_k(\phi_k-1)|\nabla\phi_3|\cos\theta_k/\sqrt{2}-\epsilon^2\nabla\cdot((1-\phi_3)\nabla\phi_k),\quad k=1,2. \qquad (2.15)
\end{aligned}$$

By taking the differentiations of Eq. (2.15) with respect to time t, we have

$$\frac{d}{dt}\int_\Omega\phi_k\,d\mathbf{x}=\int_\Omega\phi_{kt}\,d\mathbf{x}=\int_\Omega-\lambda M\left((1-\phi_3)\frac{\phi_k(\sqrt{2}\epsilon|\nabla\phi_k|-\phi_k(\phi_k-1))}{\epsilon^2}\right)d\mathbf{x}\neq0, \qquad (2.16)$$

which indicates that the system does not satisfy the total mass conservation. According to Eq. (2.6), when interfaces adhere to the hyperbolic tangent profile, the second term in Eq. (2.14) can be ignored. To ensure total mass conservation, Eqs. (2.14)-(2.15) can be

simplified to

$$\frac{\partial \phi_k}{\partial t} = M\nabla\cdot((1-\phi_3)\nabla\mu_k) + \underbrace{\lambda M\left(\nabla\cdot((1-\phi_3)\nabla\phi_k) - \frac{1}{\sqrt{2\epsilon}}\nabla\cdot\left((1-\phi_3)(1-\phi_k)\phi_k\frac{\nabla\phi_k}{|\nabla\phi_k|}\right)\right)}_{II}, \tag{2.17}$$

$$\mu_k = f(\phi_k)+\beta(\Phi)+\epsilon\phi_k(\phi_k-1)|\nabla\phi_3|\cos\theta_k/\sqrt{2}-\epsilon^2\nabla\cdot((1-\phi_3)\nabla\phi_k), \quad k=1,2, \tag{2.18}$$

where II is the correction term. If $\lambda=0$, the corrected ternary CH equations equal to the original ternary CH equations, which can be derived from Eq. (2.4). To satisfy $\phi_1(\mathbf{x},t)+\phi_2(\mathbf{x},t)+\phi_3(\mathbf{x})=1$, a Lagrange multiplier

$$\beta(\Phi) = -\frac{1}{3}\left(\sum_{k=1}^{3} f(\phi_k)+\sum_{k=1}^{2}\epsilon\phi_k(\phi_k-1)|\nabla\phi_3|\cos\theta_k/\sqrt{2}\right) \tag{2.19}$$

is used, which can be derived from

$$\begin{aligned}
0 &= \frac{\partial(\sum_{k=1}^{3}\phi_k)}{\partial t} = \sum_{k=1}^{3}\frac{\partial\phi_k}{\partial t} = M\nabla\cdot\left((1-\phi_3)\sum_{k=1}^{3}\nabla\mu_k\right)\\
&= M\nabla\cdot\Bigg((1-\phi_3)\nabla\sum_{k=1}^{2}\Big(f(\phi_k)+\beta(\Phi)+\epsilon\phi_k(\phi_k-1)|\nabla\phi_3|\cos\theta_k/\sqrt{2}\\
&\quad -\epsilon^2\nabla\cdot((1-\phi_3)\nabla\phi_k)\Big)\Bigg)+M\nabla\cdot\left((1-\phi_3)\nabla\left(\beta(\Phi)+f(\phi_3)-\epsilon^2\nabla\cdot((1-\phi_3)\nabla\phi_3)\right)\right)\\
&= M\nabla\cdot\left((1-\phi_3)\nabla\left(\sum_{k=1}^{3}f(\phi_k)+\sum_{k=1}^{3}\beta(\Phi)+\sum_{k=1}^{2}\epsilon\phi_k(\phi_k-1)|\nabla\phi_3|\cos\theta_k/\sqrt{2})\right)\right).
\end{aligned} \tag{2.20}$$

Since ϕ_3 is fixed, i.e., $\frac{\partial\phi_3}{\partial t}=0$, we can set

$$\mu_3 = f(\phi_3)+\beta(\Phi)-\epsilon^2\nabla\cdot((1-\phi_3)\nabla\phi_3. \tag{2.21}$$

Remark 2.1. It is important to note that the fixed phase ϕ_3 in Eq. (2.3) functions as a Heaviside function, signifying the fixed phase or non-fixed phases. Specifically, when in the complex domain Ω_{in}, $1-\phi_3=0$ holds. Consequently, according to Eqs. (2.17)-(2.18), $\partial\phi_k/\partial t=0$, implying that ϕ_1 and ϕ_2 remain at zero within Ω_{in}. Conversely, outside the complex domain, where $1-\phi_3=1$, ϕ_1 and ϕ_2 follow the gradient flow system. Thus, the ternary CH system with a fixed phase effectively emulates complex boundaries within the Cartesian grid.

Remark 2.2. The proposed model is designed to mitigate the inherent interface length minimization property of the CH model when in contact with a solid substrate. However, this modification no longer preserves the energy dissipation law, as a penalty term has been introduced into the CH model to enforce the interface to adhere to a hyperbolic tangent profile.

2.1 Contact angle boundary condition

In this section, we explain in more detail how our model can implicitly describe the wetting condition of binary fluids in contact with solids. We begin by examining Young's equality [41], which delineates the relationship between surface tensions and the microscale contact angle θ_1

$$\sigma_{F_1F_2}\cos\theta_1=\sigma_{SF_2}-\sigma_{SF_1}, \tag{2.22}$$

where $\sigma_{F_1F_2}$,σ_{SF_2}, and σ_{SF_1} are the surface tension coefficients at the interfaces between Fluid 1–Fluid 2, Solid–Fluid 2, and Solid–Fluid 1, respectively, as schematically shown in Fig. 1(b). On the boundary of solid domain ϕ_3, $\mathbf{n}=\nabla\phi_3/|\nabla\phi_3|$ is the unit normal vector to $\partial\Omega_{in}$ and the following condition is satisfied

$$\nabla\phi_k\cdot\mathbf{n}=-|\nabla\phi_k|\cos(\pi-\theta_k),\quad k=1,2. \tag{2.23}$$

As the equilibrium profile of ϕ_k closely resembles a hyperbolic tangent function, $|\nabla\phi_k|$ can be represented by $\phi_k(1-\phi_k)/(\sqrt{2}\epsilon)$ (see Eq. (2.6)). Therefore, we can reformulate Eq. (2.23) as

$$\epsilon^2\nabla\phi_3\cdot\nabla\phi_k+\epsilon\phi_k(\phi_k-1)|\nabla\phi_3|\cos\theta_k/\sqrt{2}=0. \tag{2.24}$$

As the right-hand side of Eq. (2.24) is zero, we assert that the terms on the left-hand side contribute negligibly, often referred to as "zero-contribution". As discussed in [38], achieving the homogeneous Neumann boundary condition entails setting a specific contact angle $\theta_k=90^\circ$.

For the Helmholtz free energy functional

$$\mathcal{E}_{CH}=\sum_{k=1}^{2}\mathcal{E}_{CH_k}=\sum_{k=1}^{2}\int_\Omega F(\phi_k)+\frac{\epsilon^2}{2}|\nabla\phi_k|^2\ d\mathbf{x}, \tag{2.25}$$

the kth chemical potential is

$$\begin{aligned}\bar{\mu}_k&=\frac{\delta\mathcal{E}_{CH_k}}{\delta\phi_k}+\beta(\Phi)\\&=f(\phi_k)-\epsilon^2\Delta\phi_k+\beta(\Phi).\end{aligned} \tag{2.26}$$

Subsequently, by integrating the contact angle boundary condition (i.e., Eq. (2.24)) into the expression of μ_k (i.e., Eq. (2.26)), we derive the following equation

$$\bar{\mu}_k=f(\phi_k)+\beta(\Phi)+\epsilon\phi_k(\phi_k-1)|\nabla\phi_3|\cos\theta_k/\sqrt{2}-\epsilon^2\nabla\cdot((1-\phi_3)\nabla\phi_k)-\epsilon^2\phi_3\Delta\phi_k, \tag{2.27}$$

where $\Delta\phi_k=\nabla\cdot((1-\phi_3)\nabla\phi_k)+\nabla\phi_3\cdot\nabla\phi_k+\phi_3\Delta\phi_k$ and Eq. (2.24) are used. Eqs. (2.26) and (2.27) are equivalent. As $\epsilon^2\phi_3\Delta\phi_k$ tends to zero when ϕ_3 approaches zero, the impact of the last term on the boundary can be neglected.

We hereby modify Eq. (2.27) to yield

$$\bar{\mu}_k=f(\phi_k)+\beta(\Phi)+\epsilon\phi_k(\phi_k-1)|\nabla\phi_3|\cos\theta_k/\sqrt{2}-\epsilon^2\nabla\cdot((1-\phi_3)\nabla\phi_k), \tag{2.28}$$

which precisely aligns with Eq. (2.18). The contact angle boundary condition can be exactly held as $\phi_3 \to 0$. The corresponding modified Helmholtz free energy functional is

$$\begin{aligned}\mathcal{E}_{CHmod}(\phi) &= \sum_{k=1}^{2} \mathcal{E}_{CHmod_k}(\phi) \\ &= \sum_{k=1}^{2} \int_\Omega \left(F(\phi_k) + \frac{\epsilon^2}{2}(1-\phi_3)|\nabla\phi_k|^2 + \epsilon\left(\frac{1}{3}\phi_k^3 - \frac{1}{2}\phi_k^2\right)|\nabla\phi_3|\cos\theta_k/\sqrt{2}\right) d\mathbf{x}.\end{aligned} \tag{2.29}$$

3 Numerical schemes

Now, we outline the numerical methodology for implementing the proposed model, as depicted by Eqs. (2.17)-(2.18), within a two-dimensional spatial domain. The extension to the three-dimensional domains is straightforward. Let $\Omega = (a,b)\times(c,d)$ be a computational domain. We define the discrete domain $\Omega^h = \{(x_i,y_j)|1 \le i \le N_x,\ 1 \le j \le N_y\}$, where $x_i = a+(i-0.5)h$, $y_j = c+(j-0.5)h$. N_x and N_y are the numbers of mesh grid. The space step is $h = (b-a)/N_x = (d-c)/N_y$. Let $\phi^n_{k,i,j}$ be an approximation of $\phi_k(x_i,y_j,n\Delta t)$, where $\Delta t = T/N_t$ is the time step, T is the final computational time, N_t is the number of time steps. To simplify the notations, d_{ij} and $c^n_{k,ij}$ are the approximations of $1-\phi_3(x_i,y_j)$ and $(1-\phi_3(x_i,y_j))(1-\phi_k(x_i,y_j,n\Delta t))\phi_k(x_i,y_j,n\Delta t)$, respectively. The second-order backward difference formula (BDF2) and the stabilization technique [47] are used to discretize Eqs. (2.17) and (2.18) as the following form

$$\begin{aligned}\frac{3\phi^{n+1}_{k,ij} - 4\phi^n_{k,ij} + \phi^{n-1}_{k,ij}}{2\partial t} &= M\nabla_d\cdot(d_{ij}\nabla_d\mu^{n+1}_{k,ij}) \\ &\quad + \lambda M\left(\nabla_d\cdot(d_{ij}\nabla_d\phi^n_{k,ij}) - \frac{1}{\sqrt{2\epsilon}}\tilde{\nabla}^c_d\cdot\left(c_{k,ij}\frac{\nabla^c_d\phi_k}{|\nabla^c_d\phi_k|}\right)^n\right),\end{aligned} \tag{3.1}$$

$$\begin{aligned}\mu^n_{k,ij} &= f(\phi^*_{k,ij}) + \beta(\Phi^*_{ij}) + \epsilon\phi^*_{k,ij}(\phi^*_{k,ij}-1)|\nabla_d\phi_{3,ij}|\cos\theta_k/\sqrt{2} - \epsilon^2\nabla\cdot(d_{ij}\nabla_d\phi^*_{k,ij}) \\ &\quad + S(\phi^{n+1}_{k,ij} - \phi^*_{k,ij}), \quad k=1,2.\end{aligned} \tag{3.2}$$

S is a positive second-order linear stabilizer used to enhance the stability of the numerical method. The explicit Adams–Bashforth (AB) approximation is used in $(\cdot)^*$, i.e., $(\cdot)^* = 2(\cdot)^n - (\cdot)^{n-1}$. The periodic boundary or the following discrete boundary conditions are considered $\nabla c^n_k\cdot\mathbf{n}|_{\partial\Omega} = \nabla\mu^n_k\cdot\mathbf{n}|_{\partial\Omega} = 0$, for $k=1,2$.

The discrete Laplacian operators $\nabla_d\cdot(d_{ij}\nabla_d\mu^{n+1}_{k,ij})$ can be given by

$$\begin{aligned}\nabla_d\cdot(d_{ij}\nabla_d\mu^{n+1}_{k,ij}) &= \frac{d_{i+1/2,j}\mu^{n+1}_{k,i+1,j} + d_{i-1/2,j}\mu^{n+1}_{k,i-1,j} + d_{i,j+1/2}\mu^{n+1}_{k,i,j+1} + d_{i,j-1/2}\mu^{n+1}_{k,i,j-1}}{h^2} \\ &\quad - \frac{d_{i+1/2,j} + d_{i-1/2,j} + d_{i,j+1/2} + d_{i,j-1/2}}{h^2}\mu^{n+1}_{k,ij},\end{aligned} \tag{3.3}$$

where $d_{i+1/2,j}=(d_{i+1,j}+d_{ij})/2$. $\nabla_d\cdot(d_{ij}\nabla_d\mu_{k,ij}^{n+1})$ and $\nabla_d\cdot(d_{ij}\nabla_d\phi_{k,ij}^{*})$ are defined in a similar manner. $|\nabla_d\phi_{3,ij}|$ is computed by the central difference scheme

$$|\nabla_d\phi_{3,ij}|=\sqrt{\left(\frac{\phi_{3,i+1,j}-\phi_{3,i-1,j}}{2h}\right)^2+\left(\frac{\phi_{3,i,j+1}-\phi_{3,i,j-1}}{2h}\right)^2}. \tag{3.4}$$

Note that $m=\nabla_d^c\phi$ is a gradient vector at the cell corner. Vertex-centered normal vectors are obtained by differentiating the phase field in the four surrounding cells. For example, the normal vector at the top right vertex of cell Ω^h is given by

$$\begin{aligned}\mathbf{m}_{i+1/2,j+1/2}&=(n_{i+1/2,j+1/2}^x,n_{i+1/2,j+1/2}^y)\\&=\left(\frac{\phi_{i+1,j}+\phi_{i+1,j+1}-\phi_{ij}-\phi_{i,j+1}}{2h},\frac{\phi_{i,j+1}+\phi_{i+1,j+1}-\phi_{ij}-\phi_{i+1,j}}{2h}\right).\end{aligned} \tag{3.5}$$

Then, the vertex-centered normal is given by

$$\begin{aligned}\nabla_d\cdot\left(\frac{\mathbf{m}}{|\mathbf{m}|}\right)_{ij}=\frac{1}{2h}\Bigg(&\frac{n_{i+1/2,j+1/2}^x+n_{i+1/2,j+1/2}^y}{|\mathbf{m}_{i+1/2,j+1/2}|}+\frac{n_{i+1/2,j-1/2}^x-n_{i+1/2,j-1/2}^y}{|\mathbf{m}_{i+1/2,j-1/2}|}\\&-\frac{n_{i-1/2,j+1/2}^x-n_{i-1/2,j+1/2}^y}{|\mathbf{m}_{i-1/2,j+1/2}|}-\frac{n_{i-1/2,j-1/2}^x+n_{i-1/2,j-1/2}^y}{|\mathbf{m}_{i-1/2,j-1/2}|}\Bigg).\end{aligned} \tag{3.6}$$

Here, we discretize the last term of Eq. (3.2) at the cell centers from the vertex-centered normal as follows

$$\begin{aligned}\tilde{\nabla}_d^c\cdot\left(c_{k,ij}\frac{\nabla_d^c\phi_k}{|\nabla_d^c\phi_k|}\right)=\frac{1}{2h}\Bigg(&c_{k,i+1/2,j+1/2}\frac{n_{i+1/2,j+1/2}^x}{\mathbf{m}_{i+1/2,j+1/2}}+c_{k,i+1/2,j-1/2}\frac{n_{i+1/2,j-1/2}^x}{\mathbf{m}_{i+1/2,j-1/2}}\\&-c_{k,i-1/2,j+1/2}\frac{n_{i-1/2,j+1/2}^x}{\mathbf{m}_{i-1/2,j+1/2}}-c_{k,i-1/2,j-1/2}\frac{n_{i-1/2,j-1/2}^x}{\mathbf{m}_{i-1/2,j-1/2}}\\&+c_{k,i+1/2,j+1/2}\frac{n_{i+1/2,j+1/2}^y}{\mathbf{m}_{i+1/2,j+1/2}}+c_{k,i+1/2,j-1/2}\frac{n_{i+1/2,j-1/2}^y}{\mathbf{m}_{i+1/2,j-1/2}}\\&-c_{k,i-1/2,j+1/2}\frac{n_{i-1/2,j+1/2}^y}{\mathbf{m}_{i-1/2,j+1/2}}-c_{k,i-1/2,j-1/2}\frac{n_{i-1/2,j-1/2}^y}{\mathbf{m}_{i-1/2,j-1/2}}\Bigg).\end{aligned} \tag{3.7}$$

The resulting nonlinear system of Eqs. (3.1) and (3.2) is solved efficiently using a nonlinear multigrid method [48].

Remark 3.1. To initiate the second-order scheme (3.1)-(3.2), we need the values of ϕ_1^1, ϕ_2^1. Here, we describe the first-order scheme for Eqs. (2.17)-(2.18). Based on the backward

Euler approach, the fully discrete scheme can be written to be

$$\frac{\phi_{k,ij}^{n+1}-\phi_{k,ij}^{n}}{\partial t}=M\nabla_d\cdot(d_{ij}\nabla_d\mu_{k,ij}^{n+1})+\lambda M\left(\nabla_d\cdot(d_{ij}\nabla_d\phi_{k,ij}^{n})-\frac{1}{\sqrt{2\epsilon}}\tilde{\nabla}_d^c\cdot\left(c_{k,ij}\frac{\nabla_d^c\phi_k}{|\nabla_d^c\phi_k|}\right)^n\right), \tag{3.8}$$

$$\begin{aligned}\mu_{k,ij}^{n}=&f(\phi_{k,ij}^{n})+\beta(\phi_{ij}^{n})+\epsilon\phi_{k,ij}^{n}(\phi_{k,ij}^{n}-1)|\nabla_d\phi_{3,ij}|\cos\theta_k/\sqrt{2}-\epsilon^2\nabla\cdot(d_{ij}\nabla_d\phi_{k,ij}^{n})\\&+S(\phi_{k,ij}^{n+1}-\phi_{k,ij}^{n}),\quad k=1,2,\end{aligned} \tag{3.9}$$

where S is a positive stabilization parameter to improve stability of the numerical method.

4 Numerical experiments

In this section, various numerical experiments have been performed to demonstrate the efficiency of the proposed method. In 2D space, we consider a comparison with the original ternary CH model, the effect of contact angle without fluid flow, and droplets in the 2D complex domain. With background fluid, the effect of contact angle with fluid flow and gravity-driven flow in a porous medium are performed. In 3D space, a comparison of original ternary CH model in 3D and droplets in the 3D complex domain is investigated. Unless otherwise, $S=2$, $\epsilon=4h/(2\sqrt{2}\tanh^{-1}(0.9))$ [43]. In the 2D case, the periodic and homogeneous Neumann boundary conditions are considered along x- and y-directions, respectively. In the 3D case, the periodic conditions are considered along x- and y-directions, and the homogeneous Neumann boundary conditions are considered along z-direction.

4.1 Comparison with original ternary CH in 2D

We consider two droplets located at the solid substrate. The initial conditions are defined to be

$$\phi_3(x,y)=0.5+0.5\tanh\left(\frac{-\max(|x-0.5|-0.45,|y+0.2|-0.5)}{2\sqrt{2}\epsilon}\right), \tag{4.1}$$

$$\begin{aligned}\psi(x,y,0)=&0.5+0.5\tanh\left(\frac{0.2-\sqrt{(x-0.3)^2+(y-0.35)^2}}{2\sqrt{2}\epsilon}\right)\\&+0.5+0.5\tanh\left(\frac{0.1-\sqrt{(x-0.75)^2+(y-0.25)^2}}{2\sqrt{2}\epsilon}\right),\end{aligned} \tag{4.2}$$

$$\phi_1(x,y,0)=\begin{cases}1-\phi_3(x,y), & \text{if } \phi_3(x,y)+\psi(x,y,0)>1,\\ \psi(x,y,0), & \text{otherwise,}\end{cases} \tag{4.3}$$

$$\phi_2(x,y,0)=1-\phi_1(x,y,0)-\phi_3(x,y), \tag{4.4}$$

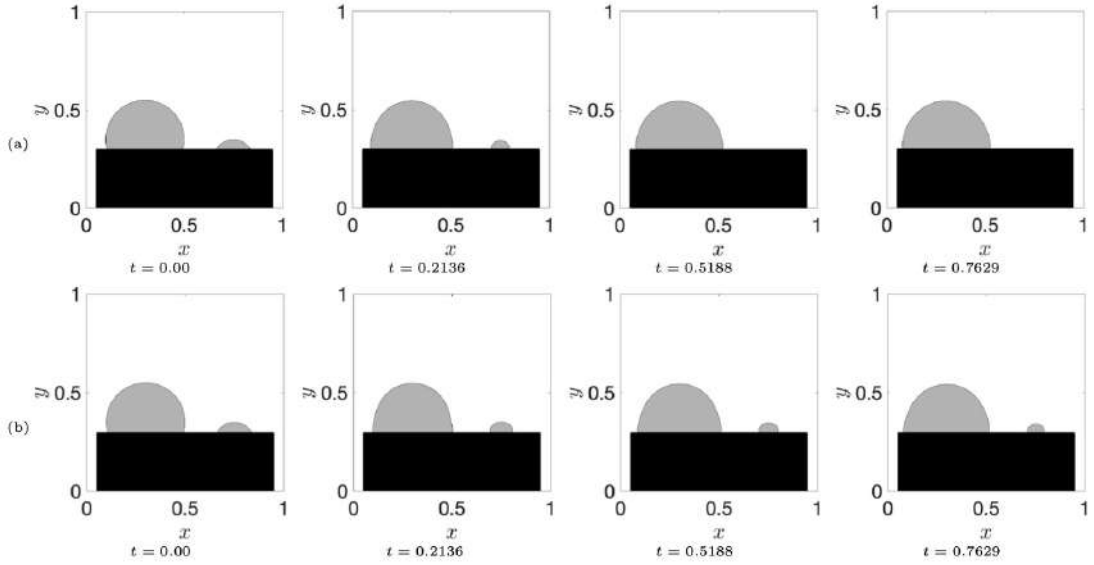

Figure 2: Temporal evolution of phase interface contacting a solid boundary for the original ternary CH equation (a) and corrected ternary CH equation (b).

on the domain $(0,1)\times(0,1)$. The parameters $h=1/128$, $\Delta t=5h^2$, $\theta_1=90^\circ$, $\lambda=0.15$ are used. Fig. 2(a) and (b) illustrate the temporal evolutions for the original ternary CH model ($\lambda=0$) and corrected ternary CH model, respectively. The solid phase is defined by ϕ_3 (black), the droplets (Fluid 1) phase are defined by ϕ_1 (gray), and the Fluid 2 phase is defined by ϕ_2 (white). The interface profiles are shown in Fig. 3. It becomes evident that when employing the original ternary CH model, the small droplet gradually shrinks and eventually vanishes, a behavior that contradicts physical expectations (Fig. 3(a)). Conversely, when the interface correction term is applied, the small droplet persists, as demonstrated in Fig. 3(b). Fig. 4 presents the temporal evolution of total mass and mass ratio for the small droplet, comparing the results obtained with both methods. Notably, both methods exhibit mass conservation properties across the entire domain. However, it is worth highlighting that the mass for the small droplet, when computed using the original ternary CH model, undergoes significant changes over time from its initial state. In contrast, our model effectively addresses and corrects the mass loss occurring within the interfacial region.

4.2 Effect of contact angle without fluid flow

In this test, we examine an equilibrium phase interface interfacing with a solid surface, with specified contact angles denoted as $\theta_1=60^\circ$ and $\theta_1=120^\circ$, symbolizing wetting and non-wetting conditions, respectively. The determination of the equilibrium state adheres to convergence criteria predicated on $|\phi_1^{n+1}-\phi_1^n|_2\leq 10^{-6}$. The corrected CH model is

(a)

(b)

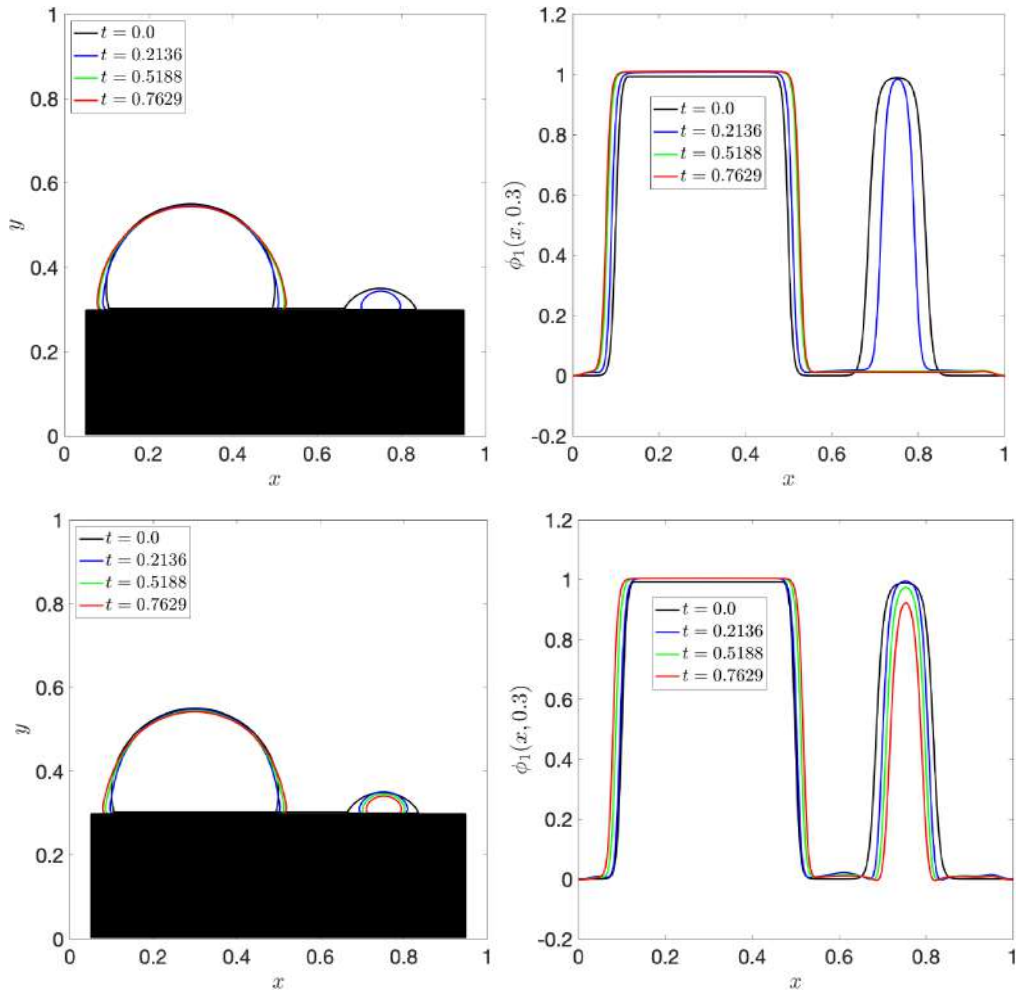

Figure 3: Mesh plots of the phase-field profiles for the original ternary CH equation (a) and proposed equation (b). The whole view is on the left, and the plane view is on the right.

numerically solved over the computational domain $\Omega=(0,2)\times(0,1)$ utilizing a grid resolution of 256×128. Additionally, the other parameters are set as $\Delta t=5h^2$ and $\lambda=0.01$. The initial conditions are specified as follows

$$\phi_3=0.5+0.5\tanh\left(\frac{-\max(|x-0.75|-0.75,|y-0.5|-(x/6-0.01))}{0.5\sqrt{2}\epsilon}\right), \tag{4.5}$$

$$\phi_1(x,y,0)=(1-\phi_3)\left(0.5+0.5\tanh\left(\frac{-\max(|x-0.75|-0.3,|y-0.5|-0.28)}{0.5\sqrt{2}\epsilon}\right)\right), \tag{4.6}$$

$$\phi_2(x,y,0)=1-\phi_1(x,y,0)-\phi_3(x,y). \tag{4.7}$$

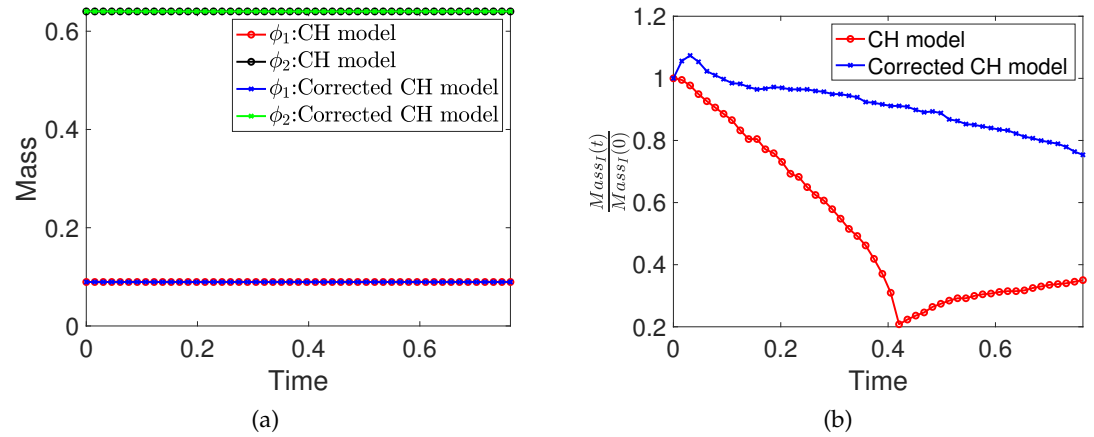

Figure 4: (a) Temporal evolution of the mass. (b) Temporal evolution of the mass ratio for the small drop.

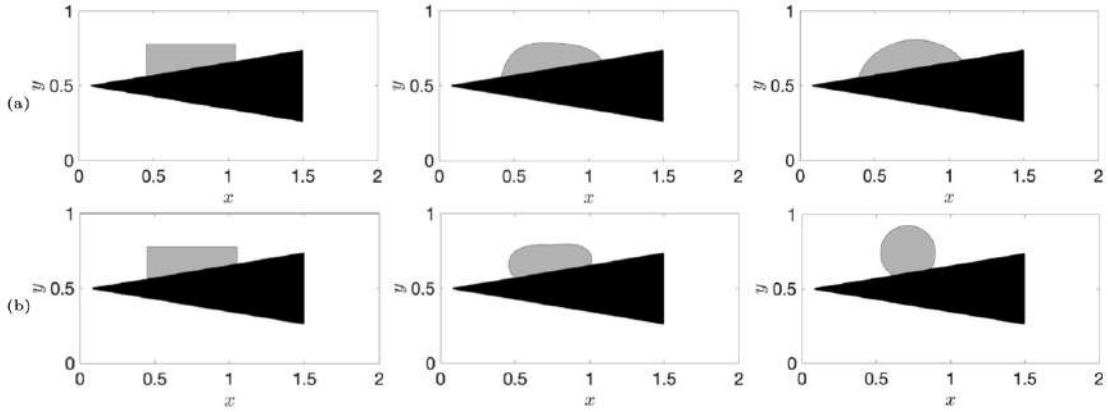

Figure 5: Temporal evolution with respect to different contact angles: (a) $\theta_1=60^\circ$and (b) $\theta_1=150^\circ$. The times from left to right in each row are: $t=0$, 0.3052, 8.5449 (equilibrium state).

Fig. 5(a) and (b) illustrate the temporal evolution with respect to different contact angles $\theta_1=60^\circ$ and $\theta_1=150^\circ$, respectively. The solid phase is defined by ϕ_3 (black), the Fluid 1 phase is defined by ϕ_1 (gray), and the Fluid 2 phase is defined by ϕ_2 (white). We can find that an initial phase evolves to a specific pattern with respect to different θ_1. Table 1 lists the exact contact angles and numerical contact angles. These numerical angles are computed following a similar procedure in [49]. Numerical values 1 and 2 are computed using the original ternary CH model and the corrected ternary CH model, respectively. It is evident that the results obtained from the improved ternary CH model closely align with the prescribed contact angles, in contrast to the outcomes generated by the original ternary CH model. The associated snapshots at the final stage are visually presented in Fig. 6, with a close-up view provided in the right column.

Table 1: Comparison between the numerical and exact contact angles.

Exact value	60°	150°
Numerical value 1	60.97°	147.90°
Numerical value 2	59.41°	148.49°

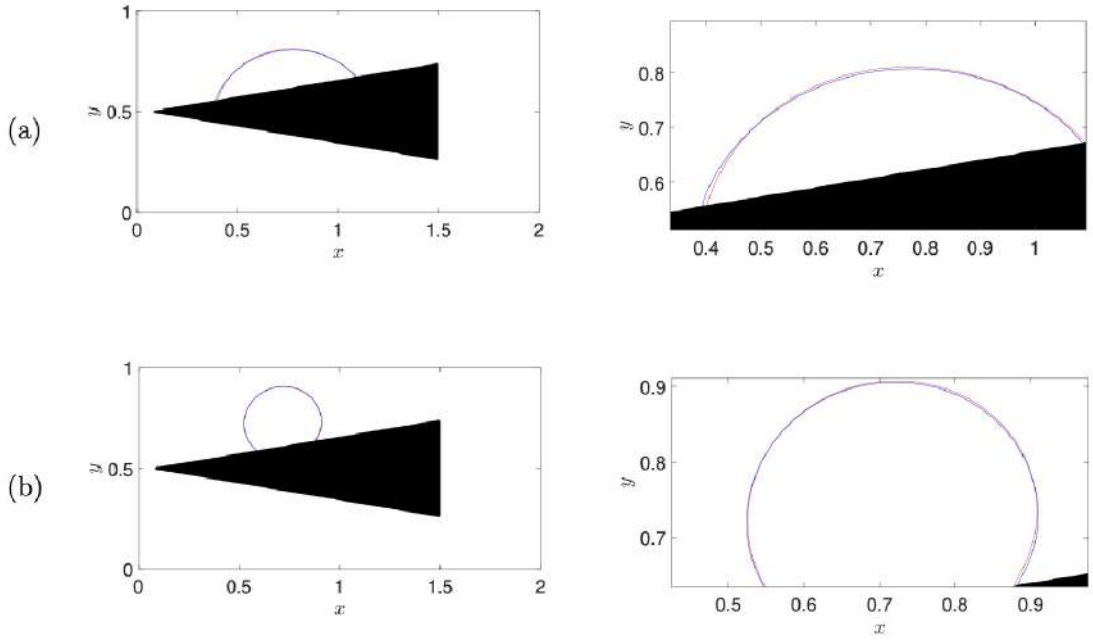

Figure 6: Comparisons of equilibrium state under (a) $\theta=60^\circ$ and (b) $\theta=150^\circ$ obtained by different ternary CH model. The red lines are the results obtained by the original ternary CH model. The blue lines are the results obtained by the corrected ternary CH model. The right column is close-up views.

4.3 Droplets in 2D complex domain

The parameters $h=1/256$, $\Delta t=5h^2$, $\lambda=0.15$ are used. Fig. 7(a) and (b) illustrate the final state results (i.e., $t=0.0443$) obtained using the original ternary CH model and corrected ternary CH model, respectively, for varying contact angles $\theta=30^\circ$, 90°, 150°.The outcomes from these experiments affirm that the proposed model effectively preserves intricate geometric features.

4.4 The corrected ternary CH system with background fluid

To verify the robustness of the proposed ternary CH system in a complex domain, we introduce convection terms into Eq. (2.18). These terms enable the phase interfaces to be advected by a prescribed background velocity field denoted as **u**. By integrating the

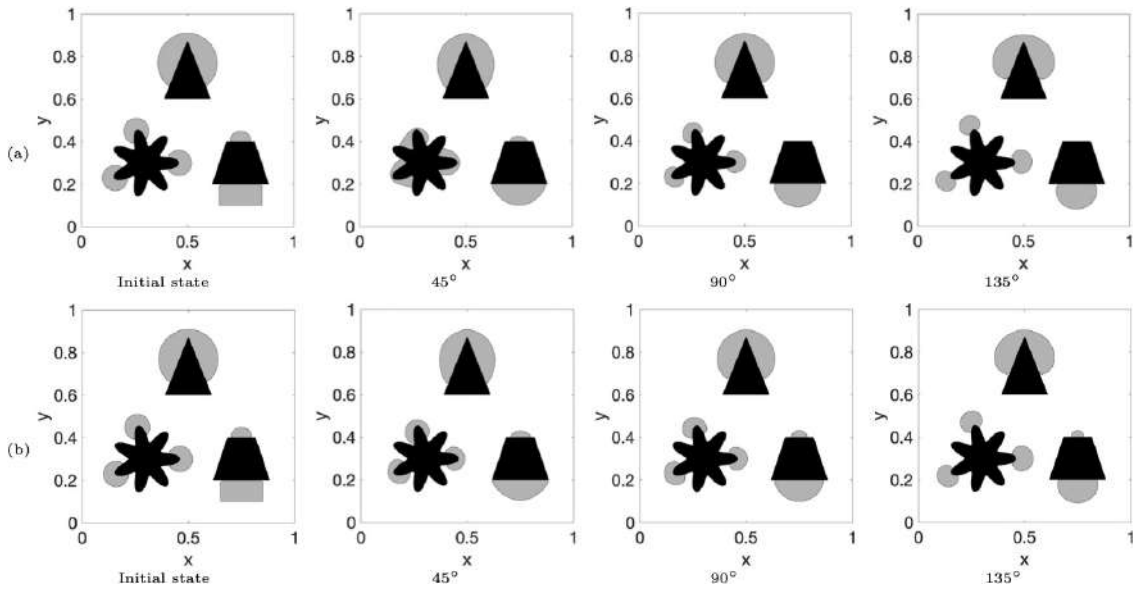

Figure 7: Droplets in a complex domain at $t=0.0443$ with respect to $\theta_1=45^\circ$, 90°, 135° obtained by the original ternary CH model (a) and corrected ternary CH model (b), respectively.

incompressible Navier-Stokes (NS) equations, we formulate an incompressible ternary CHNS system

$$\rho^*\left(\frac{\partial \mathbf{u}}{\partial t}+\mathbf{u}\cdot\nabla\mathbf{u}\right)=-\nabla p+\frac{1}{Re}\Delta\mathbf{u}+\frac{1}{We}\mathbf{SF}+(\rho(\mathbf{\Phi})-\rho^*)\mathbf{g}, \tag{4.8}$$

$$\nabla\cdot\mathbf{u}=0, \tag{4.9}$$

$$\begin{aligned}\frac{\partial \phi_k}{\partial t}+\nabla\cdot(\phi_k\mathbf{u})&=\frac{1}{Pe}\nabla\cdot((1-\phi_3)\nabla\mu_k)\\&\quad+\lambda M\left(\nabla\cdot((1-\phi_3)\nabla\phi_k)-\frac{1}{\sqrt{2\epsilon}}\nabla\cdot\left((1-\phi_3)(1-\phi_k)\phi_k\frac{\nabla\phi_k}{|\nabla\phi_k|}\right)\right),\end{aligned} \tag{4.10}$$

$$\mu_k=f(\phi_k)+\beta(\Phi)+\epsilon\phi_k(1-\phi_k)|\nabla\phi_3|\cos\theta_k/\sqrt{2}-\epsilon^2\nabla\cdot((1-\phi_3)\nabla\phi_k),\quad k=1,2, \tag{4.11}$$

where $\mathbf{u}$, p are the velocity, pressure, respectively. Pe, Re and We are the P'eclet number, Reynolds number and Weber number, respectively. We set $\rho(\mathbf{\Phi})=\rho_1\phi_1+\rho_2\phi_2$, where ρ_1, ρ_2 are the densities of ϕ_1, ϕ_2. The background density is set as a constant $\rho^*=\rho_2$. The gravitational force is $\mathbf{g}$. The surface tension is defined as [23]

$$\mathbf{SF}=-6\sqrt{2}\epsilon\sum_{k=1}^{2}\nabla\cdot\left(\frac{\nabla\phi_k}{|\nabla\phi_k|}|\nabla\phi_k|\nabla\phi_k\right). \tag{4.12}$$

In this paper, we adopted an augmented projection method for computing flows with complex boundaries proposed by Kim [50].

4.4.1 Effect of contact angle with fluid flow

In this investigation, we explore the influence of contact angle in the presence of fluid flow, as illustrated in Fig. 9(a). In this representation, the triangular-shaped solid domain is characterized by ϕ_3 (in black), the droplet is represented by ϕ_1 (in gray), and the continuous fluid phase is delineated by ϕ_2 (in white). Within the spatial domain $\Omega=(0,4)\times(0,1)$, the initial conditions are specified as follows

$$\phi_3=0.5+0.5\tanh\left(\frac{-\max(|x-2.25|-0.75,|y-0.5|-(x/6-0.25))}{\sqrt{2}\epsilon}\right), \tag{4.13}$$

$$\phi_1(x,y,0)=(1-\phi_3)\left(0.5+0.5\tanh\left(\frac{0.25-\sqrt{(x-1)^2+(y-0.5)^2}}{\sqrt{2}\epsilon}\right)\right), \tag{4.14}$$

$$\phi_2(x,y,0)=1-\phi_1(x,y,0)-\phi_3(x,y), \tag{4.15}$$

$$u(x,y,0)=1.0,\quad v(x,y,0)=0,\quad p(x,y,0)=0. \tag{4.16}$$

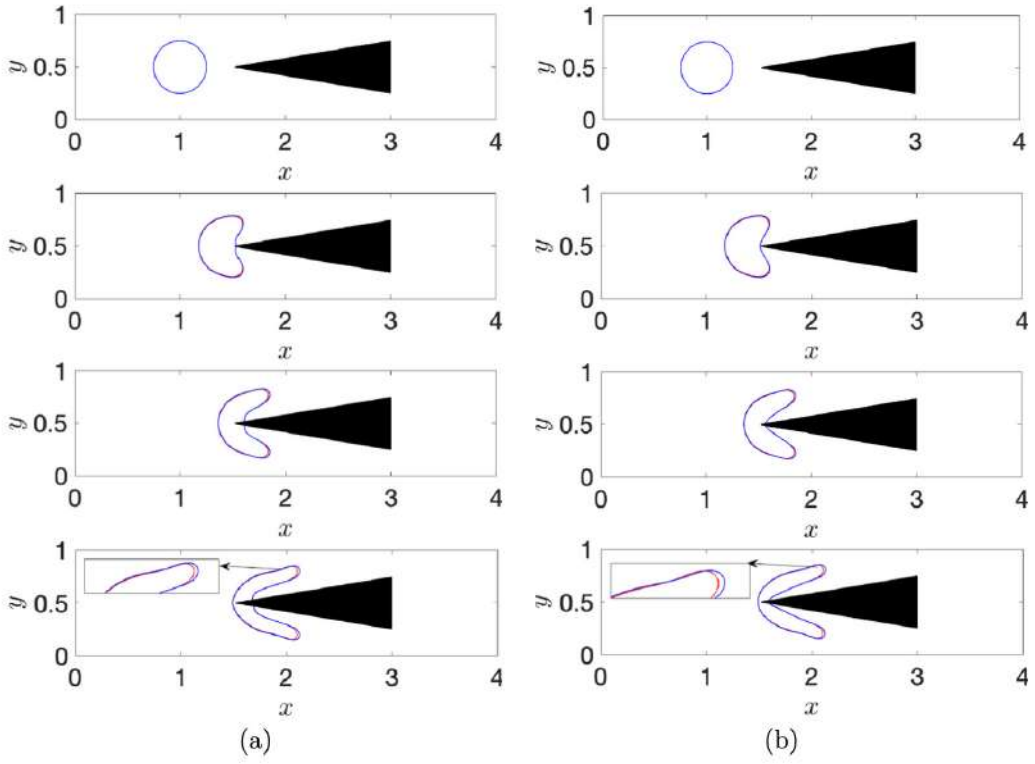

Figure 8: Temporal evolution of a droplet passing a triangle-shaped solid structure for (a) $\theta_1=30^\circ$ and (b) $\theta_1=150^\circ$, respectively. The times from the top to bottom in each column are: $t=0$, 2.3193, 3.5400, 4.7607. The red lines are the results obtained by the original ternary CH model. The blue lines are the results obtained by the corrected ternary CH model. The insets are close-up views.

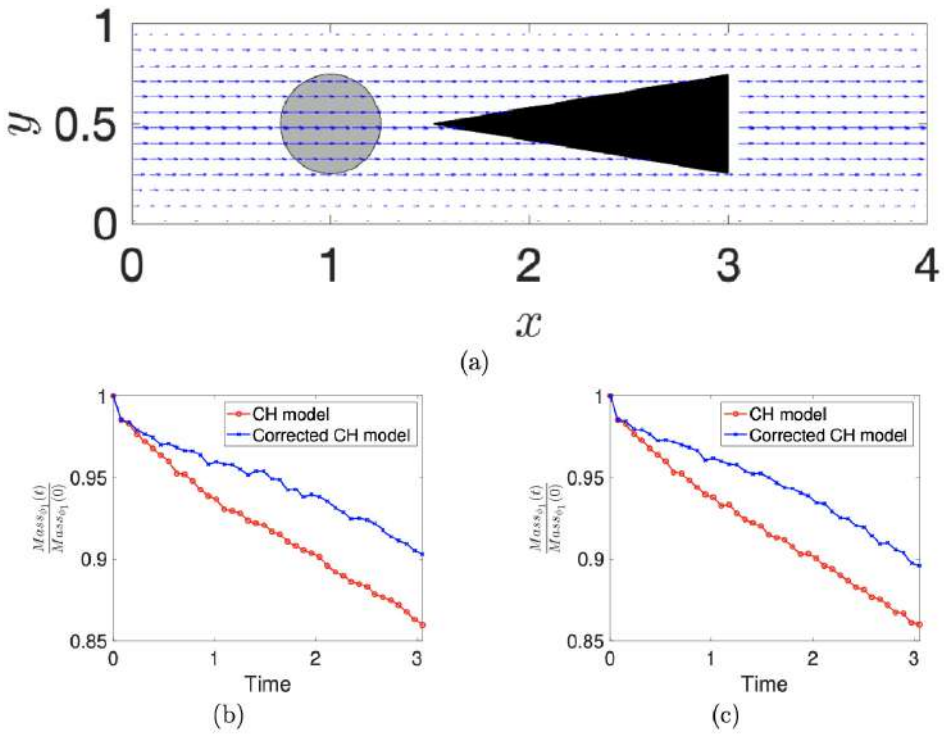

Figure 9: (a) Initial state. Temporal evolution of the mass ratio for the ϕ_1 for (b) $\theta=30^\circ$ and (c) $\theta=150^\circ$, respectively.

The boundary conditions for the u, v at y-direction are set as follows

$$u|_{x=0}=3y(1-y), \quad \mathbf{n}\cdot\nabla u|_{x=4}=0,$$
$$v|_{x=0}=0, \quad v|_{x=4}=0.$$

We use no slip boundary condition for the u, v at x-direction. The homogeneous Neumann conditions are given for phase-field variables and pressure. The background flow field is shown in Fig. 9(a). The parameters $h=1/128$, $\Delta t=10h^2$, $Re=1$, $We=10$, $Pe=0.1/\epsilon$, $\lambda=0.03$, $\rho_1=\rho_2=1$ are used. The effect of gravity is ignored (i.e. $\mathbf{g}=(0,0)$).

In Fig. 8(a) and (b), we depict the temporal progression of a droplet navigating past a triangle-shaped solid structure, considering contact angles of $\theta_1=30^\circ$ and $\theta_1=150^\circ$, respectively. These visualizations enable us to discern wetting and non-wetting processes associated with $\theta_1=30^\circ$ and $\theta_1=150^\circ$, respectively. The results obtained using the original ternary CH model and the proposed model are represented by red and blue lines, respectively. Evidently, the proposed model excels in preserving the area of the droplet, as also evidenced in Fig. 9(b) and (c). Fig. 9(b) and (c) further illustrate the temporal evolution of the mass ratio for ϕ_1 under contact angles of $\theta=30^\circ$ and $\theta=150^\circ$, respectively.

4.4.2 Gravity-driven flow in a porous medium

The phase-field method has gained extensive utilization in the investigation of transport phenomena within porous media [51], primarily due to its capacity to provide precise insights into flow physics, particularly when dealing with intricate moving interfaces and complex topological structures. In this context, we examine two-phase flows within a simulated porous medium, as showed in Fig. 11(a). The porous region, comprised of multiple circular structures, is represented by ϕ_3. Let us establish the initial conditions as follows

$$\phi_1(x,y,0)=(1-\phi_3)\left(0.5+0.5\tanh\left(\frac{-\max(|y-0.75|-0.08,|x|-0.4)}{2\sqrt{2}\epsilon}\right)\right), \tag{4.17}$$

$$v(x,y,0)=\frac{5}{2}\left(\tanh\left(\frac{-\max(|y-0.75|-0.08,|x|-0.4)}{2\sqrt{2}\epsilon}\right)+1\right), \tag{4.18}$$

$$u(x,y,0)=0, \quad p(x,y,0)=0, \tag{4.19}$$

on the whole computational domain $\Omega=[-0.5,0.5]\times[-1,1]$ with a uniform grid 256×512. We set the no-slip condition for velocities on the porous region, i.e., $\mathbf{u}^{n+1}|_{\partial\Omega}=0$. The homogeneous Neumann conditions are given for phase field variables and pressure. The background flow field, as shown in Fig. 11(a). The other numerical parameters are set as follows: Re=100, ρ_1:ρ_2=2:1, $\mathbf{g}$=(0,10), θ=90°, λ=0.15, $\Delta t=100h^2$, $Pe=0.1/\epsilon$. Notably, for this particular simulation, the impact of the surface tension force is disregarded, meaning that $We=\infty$. Fig. 10(a) and (b) illustrate the temporal evolution of gravity-driven flow within a porous medium, as computed using the original ternary CH equation and the corrected ternary CH equation, respectively. As we can see, under the combined influences of convection and boundary collisions, the droplet undergoes fragmentation, resulting in the formation of multiple segments. To facilitate a comparative assessment of the two models, Fig. 10(c) presents a side-by-side comparison, clearly indicating that the corrected ternary CH model excels in capturing more intricate geometric features of the interfaces. Furthermore, Fig. 11(b) presents the temporal evolution of the mass ratio for ϕ_1, underscoring the improved ability of the corrected ternary CH model to preserve local mass compared to the original CH equation.

4.5 Comparison with original CH in 3D

In this example, we investigate the behavior of a droplet on the rectangular solid, as represented in Fig. 12. The computational domain is defined as $\Omega=[0,1]\times[0,1]\times[0,1]$,

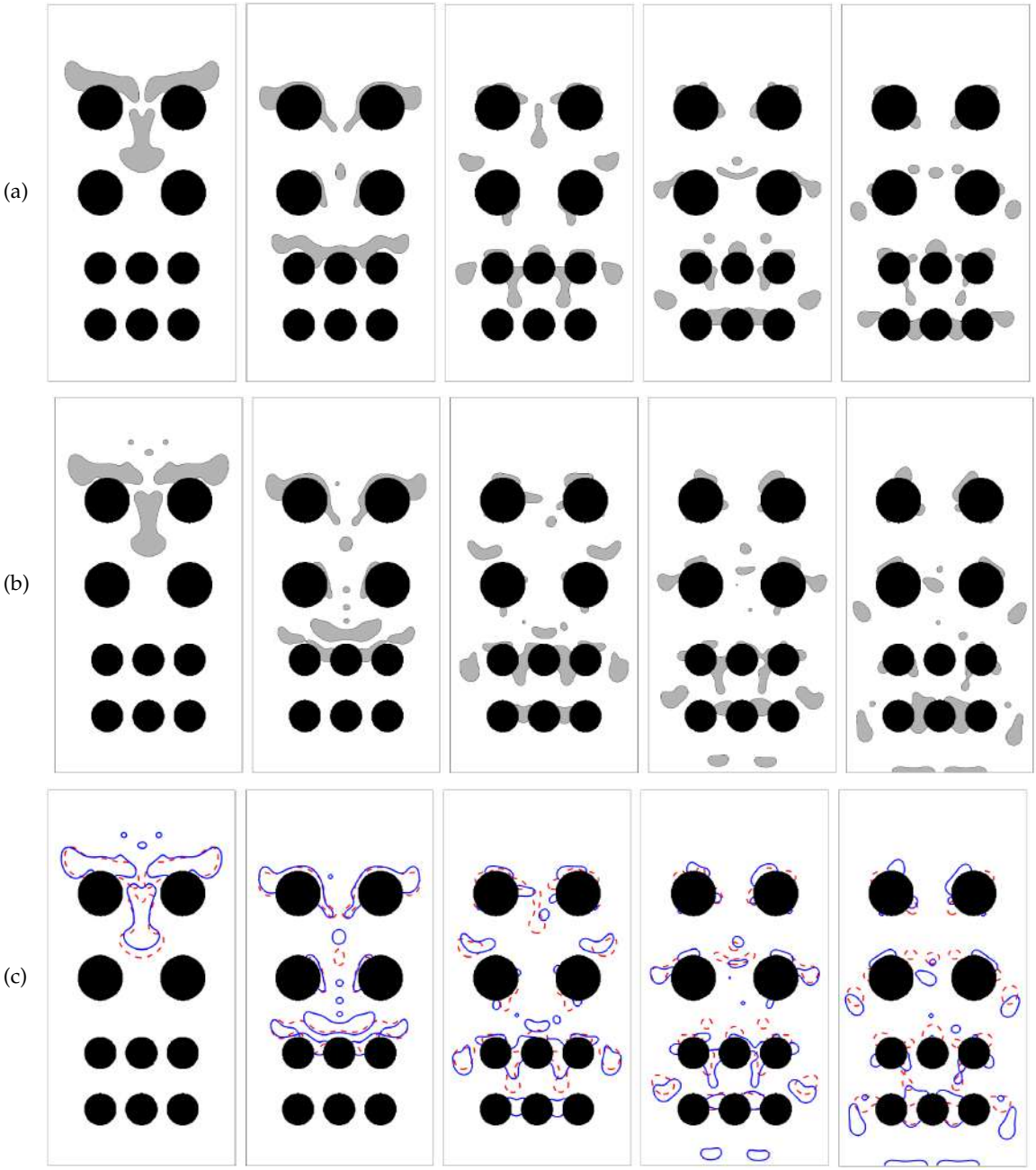

Figure 10: Temporal evolution of gravity-driven flow in a porous medium for (a) the original ternary CH equation, (b) the corrected ternary CH equation. Comparisons of gravity-driven flow in a porous medium between the CH model and the corrected ternary CH model are in (c). The red dash lines and blue solid lines are the results obtained by the original ternary CH model and the corrected ternary CH model, respectively. The times from the left to right in each row are: $t=1.6785$, 2.8992, 4.4250, 5.1880, 5.9509.

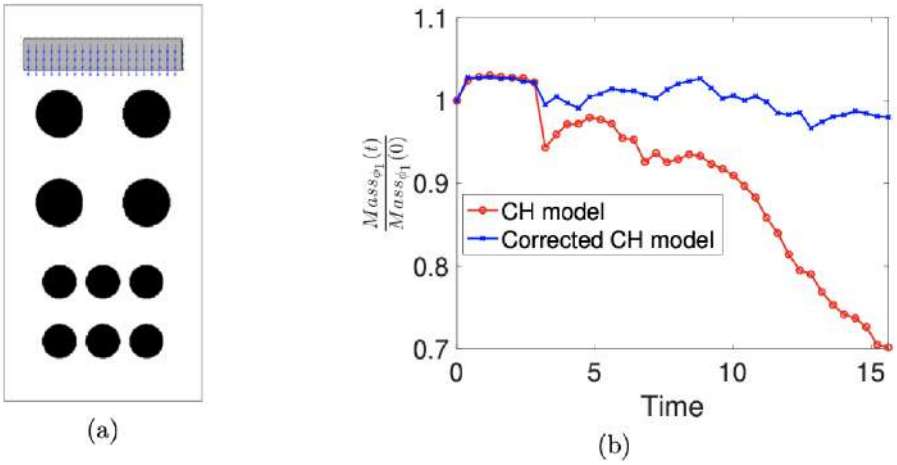

Figure 11: (a) Initial state. (b) Temporal evolution of the mass ratio for the ϕ_1.

with a discretized mesh size of $64\times64\times64$. The initial conditions are specified as follows:

$$\phi_3(x,y,z)=0.5+0.5\tanh\left(\frac{-\max(\max(|x-0.5|-0.35,|y-0.5|-0.35),|z+0.2|-0.5)}{1.6\sqrt{2}\epsilon}\right), \tag{4.20}$$

$$\phi_1(x,y,z,0)=(1-\phi_3(x,y,z))\left(0.5+0.5\tanh\left(\frac{0.3-\sqrt{(x-0.5)^2+(y-0.5)^2+(z-0.2)^2}}{0.8\sqrt{2}\epsilon}\right)\right), \tag{4.21}$$

$$\phi_2(x,y,z,0)=1-\phi_3(x,y,z)-\phi_1(x,y,z,0). \tag{4.22}$$

The parameters are set as $\Delta t=0.01$, $\theta_1=150^\circ$, $\lambda=0.15$. Fig. 12(a) and (b) illustrate the temporal evolution for the original ternary CH model and the corrected ternary CH model, respectively. The solid phase is represented by ϕ_3 (in red), the droplet is denoted as ϕ_1 (in green), and the continuum phase is symbolized by ϕ_2 (in white). Cross-sectional views at $t=0.95$ are provided in Fig. 13(a), distinctly showcasing the capacity of the corrected ternary CH model to rectify mass loss within the interfacial region. Fig. 13(b) and (c) further elucidate the temporal evolution of total mass and mass ratio for ϕ_1 using both methods. Notably, both approaches demonstrate sound mass conservation properties across the entire domain. Nevertheless, it is evident that the proposed model significantly mitigates mass loss for ϕ_1, whereas the original ternary CH model experiences substantial mass loss for the same phase.

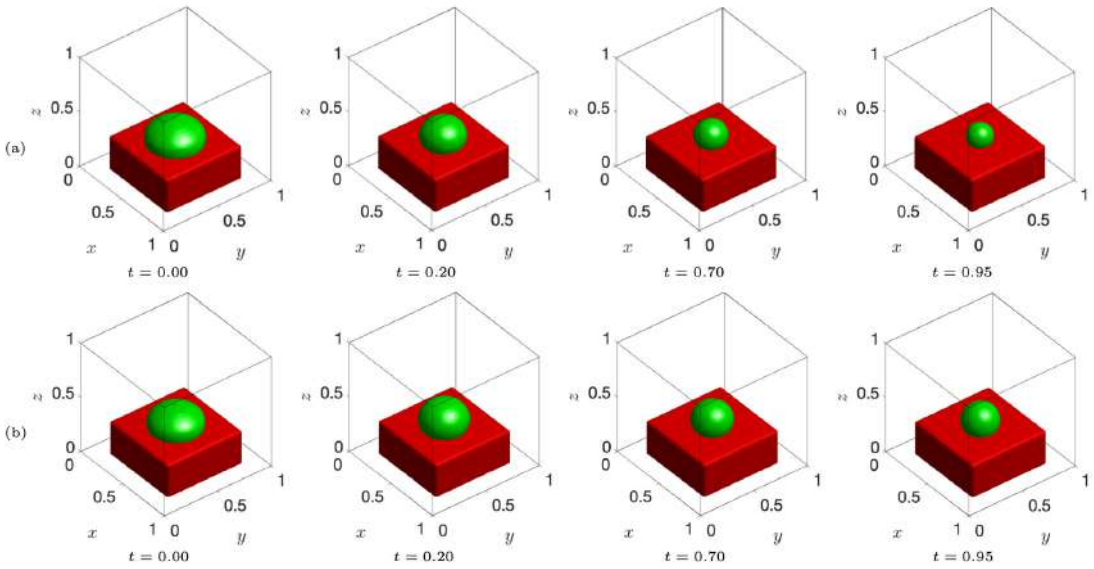

Figure 12: Temporal evolution of phase interface contacting a solid boundary for (a) the original ternary CH equation and (b) proposed equation.

4.6 Droplets in 3D complex domain

We close with an investigation of a rectangular prism-shaped droplet positioned on an ellipsoid with different contact angles $\theta_1=30^\circ$, 90°, 150°. The initial state is shown in Fig. 14. The initial conditions are considered as

$$\phi_3(x,y,z)=0.5+0.5\tanh\left(\frac{1-\sqrt{(\frac{x-0.5}{0.25})^2+(\frac{y-0.5}{0.45})^2+(\frac{z-0.26}{0.25})^2}}{2\sqrt{2}\epsilon}\right), \tag{4.23}$$

$$\phi_1(x,y,z,0)=(1-\phi_3(x,y,z)) \left(0.5+0.5\tanh\left(\frac{-\max(\max(|x-0.5|-0.18,|y-0.5|-0.18),|z-0.5|-0.19)}{\sqrt{2}\epsilon}\right)\right), \tag{4.24}$$

$$\phi_2(x,y,z,0)=1-\phi_1(x,y,z,0)-\phi_3(x,y,z). \tag{4.25}$$

The whole computational domain is defined as $\Omega=[0,1]\times[0,1]\times[0,1]$. Employing a spatial discretization with $h=1/64$, a temporal step size of $\Delta t=0.01$, and $\lambda=0.15$, we present computational results in Fig. 15 for varying contact angles, specifically $\theta_1=30^\circ$, 90°, 150°. The cross sections at $y=0.5$ and $t=0.75$ are highlighted in the right column of the figure. Notably, the impact of contact angle on the dynamic evolution of the solid boundaries is prominently displayed.

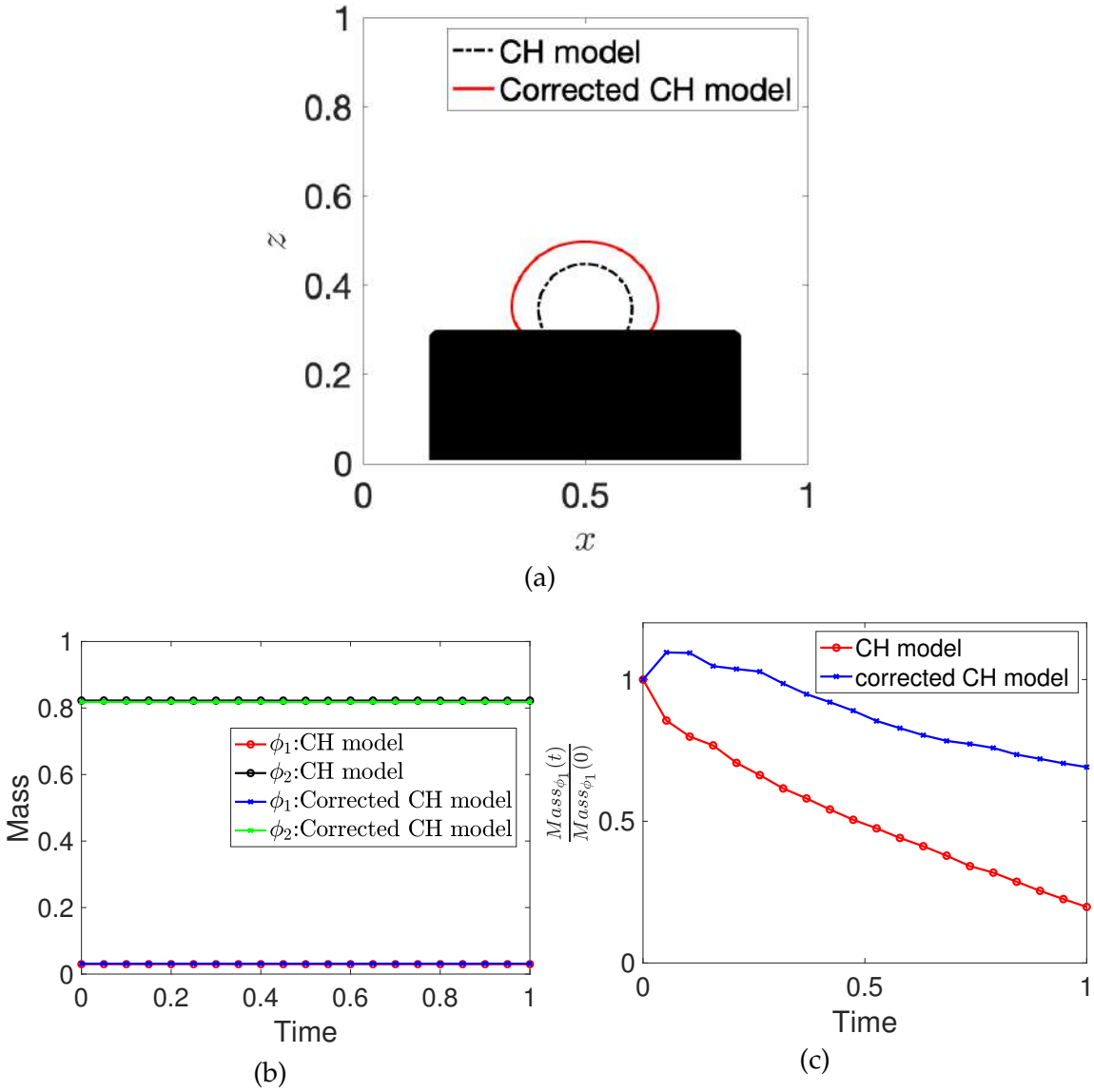

Figure 13: (a) Cross sections at $y=0.5$, $t=0.95$. (b) Temporal evolution of the mass. (c) Temporal evolution of the mass ratio for ϕ_1.

5 Conclusion

This paper presented an efficient phase-field model specifically designed for a ternary CH system, tailored to incorporate contact angle conditions within complex domains. The importance of an interface with a hyperbolic tangent profile lied in the derivation of the contact angle term from Young's equality and the hyperbolic tangent profile of the

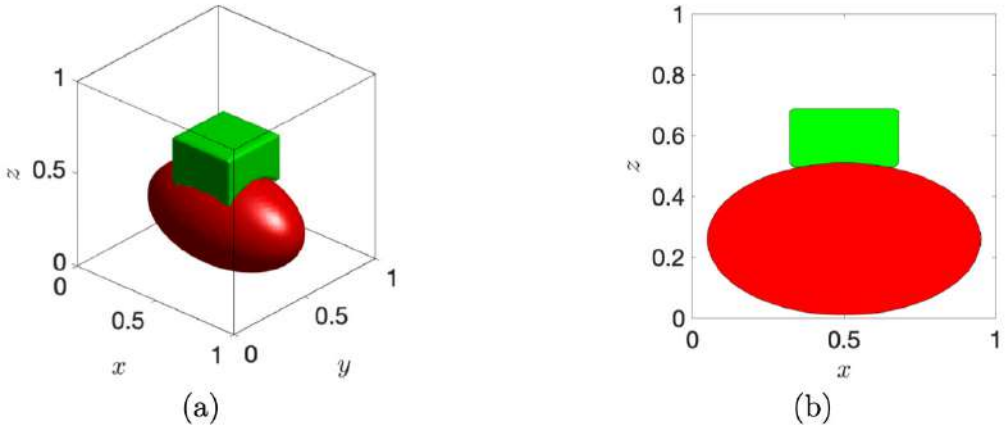

Figure 14: (a) Initial state. (b) Cross section at $y=0.5$.

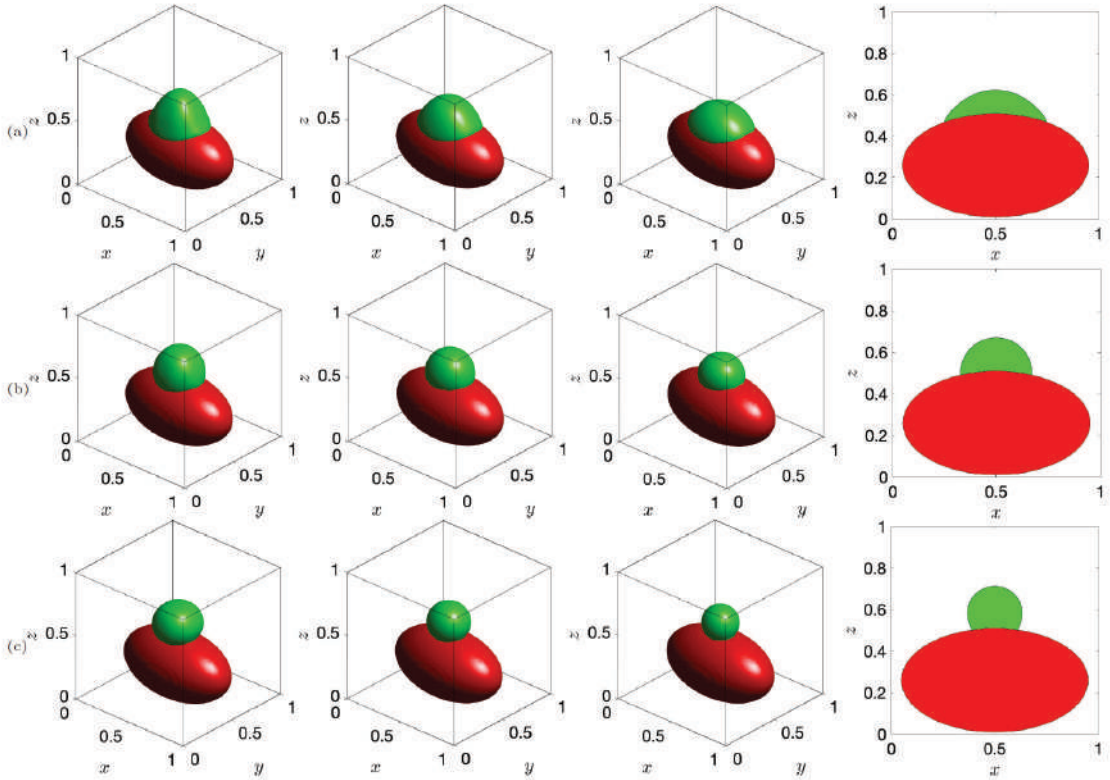

Figure 15: Temporal evolution of a droplet in the complex domain with different contact angle (a) 30°, (b) 90°, (c) 150°. The times from left to right in each row are: $t=0.0$, 0.25, 0.5, 0.75.

equilibrium interface. The inherent interface length minimization property of the original ternary CH model may result in a non-hyperbolic tangent profile for the interface between two phases, leading to inaccurate contact angle effects and mass loss within the enclosed area. To address this, a fidelity energy functional was integrated into the total energy functional, and by minimizing this part, an interface correction term was derived to enforce a hyperbolic tangent profile for the interface of the two phases. The algorithm devised for solving the corrected ternary CH model was formulated in a semi-implicit manner utilizing the BDF2 scheme. The resulting nonlinear discrete equations were solved using a nonlinear multigrid method. Computational results included comparisons with the original ternary CH model, examination of the contact angle effect without fluid flow, droplet behavior in a 2D complex domain, analysis of contact angle effects with fluid flow, and investigation of gravity-driven flow in a porous medium. Additionally, comparisons with the original ternary CH model in 3D and droplet behavior within a 3D complex domain collectively underscored the corrected ternary CH model's ability to enforce the desired hyperbolic tangent interface property, improve the contact angle effect, and reduce mass loss in each phase.

Acknowledgments

The work of Z. Tan is supported by the National Natural Science Foundation of China (Grant No. 12371418), the Guangdong Natural Science Foundation (Grant No. 2022A1515010426, Grant No. 2024A1515010694), and the Guangdong Province Key Laboratory of Computational Science at Sun Yat-sen University (Grant No. 2020B1212060032). The authors would like to thank Junxiang Yang for his very helpful comments on this paper. The authors are also grateful for the reviewers whose valuable suggestions and comments have significantly improved the quality of this paper.

References

[1] J.W. Cahn, J.E. Hilliard, Free energy of a nonuniform system. I. Interfacial free energy, J. Chem. Phys., 28 (1958) 258–67.
[2] J. Wu, X. Zhang, Z. Tan, An unconditionally energy stable algorithm for copolymer-homopolymer mixtures, Int. J. Mech. Sci., (2022) 107846.
[3] Q. Li, L. Mei, Efficient, decoupled, and second-order unconditionally energy stable numerical schemes for the coupled Cahn–Hilliard system in copolymer/homolymer mixtures, Comput. Phys. Commun., 260 (2021) 107290.
[4] J. Yang, C. Lee, D. Jeong, J. Kim, A simple and explicit numerical method for the phase-field model for diblock copolymer melts, Comput. Mater. Sci., 205 (2022) 111192.
[5] Y. Qin, C. Wang, Z. Zhang, A positivity-preserving and convergent numerical scheme for the binary fluid-surfactant system, (2021) arXiv preprint arXiv:2102.08105.
[6] G. Zhu, J. Kou, J. Yao, A. Li, S. Sun, A phase-field moving contact line model with soluble surfactants, J. Comput. Phys.J. Comput. Phys., 405 (2020) 109170.

[7] Z. Tan, Y. Tian, J. Yang, Y. Wu, J. Kim, An energy-stable method for a phase-field surfactant model, Int. J. Mech. Sci., 233 (2022) 107648.
[8] J. Yang, Phase field modeling and computation of multi-component droplet evaporation, Comput. Methods Appl. Mech. Engrg., 401 (2022) 115675.
[9] C. Zhang, H. Ding, P. Gao, Y. L. Wu, Diffuse interface simulation of ternary fluids in contact with solid, J. Comput. Phys., 309 (2016) 37–51.
[10] L. de Sobrino, J. Peternelj, On capillary waves in the gradient theory of interfaces, Can. J. Phys., 63 (1985) 131–134.
[11] S. Wise, J. Lowengrub, V. Cristini, An adaptive multigrid algorithm for simulating solid tumor growth using mixture models, Math. Comput. Model, 53(1-2) (2011) 1–20.
[12] S. Wise, J. Lowengrub, H. Frieboes, V. Cristini, Three-dimensional multispecies nonlinear tumor growth: I. Model and numerical method, J. Theor. Biol., 253 (2008) 524–543.
[13] A. Bertozzi, S. Esedoglu, A. Gillette, Inpainting of binary images using the Cahn–Hilliard equation, IEEE Trans. Image Process., 16 (2007) 285–291.
[14] Q. Yu, Q. Yu, K. Wang, B. Xia, Y. Li, First and second order unconditionally energy stable schemes for topology optimization based on phase field method, Appl. Math. Comput., 405 (2021) 126267.
[15] A. Vian, B. Reuse, E. Amstad, Scalable production of double emulsion drops with thin shells, Lab. Chip, 18 (2018) 1936–194.
[16] Y. Fu, S. Zhao, L. Bai, Y. Jin, Y. Cheng, Numerical study of double emulsion formation in microchannels by a ternary lattice boltzmann method, Chem. Eng. Sci., 146 (2016) 126–34.
[17] C. Zhang, H. Li, X. Zhang, L. Ju, Linear and unconditionally energy stable schemes for the multi-component two-phase diffuse interface model with Peng-Robinson equation of state, Commun. Comput. Phys., 26(4) (2019) 1071–1097.
[18] A. Yun, Y. Li, J. Kim, A new phase-field model for a water-oil-surfactant system, Appl. Math. Comput., 229 (2014) 422–432.
[19] T. Teramoto, F. Yonezawa, Droplet growth dynamics in a water-oil-surfactant system, J. Colloid Inter. Sci., 235 (2001) 329–333.
[20] P. Shanthraj, C.Liu, A. Akbarianb, B.Svendsenb, D.Raabeb, Multi-component chemo-mechanics based on transport relations for the chemical potential, Comput. Methods Appl. Mech. Engrg., 365 (2020) 113029.
[21] D. de Fontaine, A computer simulation of the evolution of coherent composition variations in solid solutions, Ph.D. Thesis, Northwestern University, 1967.
[22] J.E. Morral, J.W. Cahn, Spinodal decomposition in ternary systems, Acta Metall., 19 (1971) 1037–1045.
[23] J. Kim, A generalized continuous surface tension force formulation for phase-field models for multi-component immiscible fluid flows, Comput. Methods Appl. Mech. Engrg., 198 (2009) 3105–3112.
[24] H.G. Lee, J. Kim, Buoyancy-driven mixing of multi-component fluids in two-dimensional tilted channels, Eur. J. Mech. B Fluids, 42 (2013) 37–46.
[25] J. Zhang, H. Liu, H. Ding, Head-on collision of two immiscible droplets of different components, Phys. Fluids, 32(8) (2020) 082106.
[26] R. Kalantarpour, A. Ebadi, S. M. Hosseinalipour, H.Liang,Three-component phase-field Lattice Boltzmann method with high density ratio and ability to simulate total spreading states, Comput. Fluids, 204 (2020) 104480.
[27] Y. Li, R. Liu, Q. Xia, C. He, Z. Li, First-and second-order unconditionally stable direct discretization methods for multi-component Cahn–Hilliard system on surfaces, J. Comput.

Appl. Math., 401 (2022) 113778.
[28] Q. Xia, Q. Yu, Y. Li, A second-order accurate, unconditionally energy stable numerical scheme for binary fluid flows on arbitrarily curved surfaces, Comput. Methods Appl. Mech. Engrg., 384 (2021) 113987.
[29] Z. Tan, J. Wu, J. Yang, Efficient and practical phase-field method for the incompressible multi-component fluids on 3D surfaces with arbitrary shapes, J. Comput. Phys., 467 (2022) 111444.
[30] J. Yang, J. Wang, Z. Tan, A simple and practical finite difference method for the phase-field crystal model with a strong nonlinear vacancy potential on 3D surfaces, Comput. Math. Appl., 121 (2022) 131–144.
[31] D. Jeong, Y. Li, C. Lee, J. Yang, J. Kim, A conservative numerical method for the Cahn–Hilliard equation with generalized mobilities on curved surfaces in three-dimensional space, Commun. Comput. Phys., 27 (2) (2020) 412–430.
[32] C. Lehrenfeld, M.A. Olshanskii, X. Xu, A stabilized trace finite element method for partial differential equations on evolving surfaces, SIAM J. Numer. Anal., 56 (2018) 1643–1672.
[33] M.A. Olshanskii, X. Xu, A trace finite element method for PDEs on evolving surfaces, SIAM J. Sci. Comput., 39 (2017) 1301–1319.
[34] D. Jeong, J. Yang, J. Kim, A practical and efficient numerical method for the Cahn–Hilliard equation in complex domains, Commun. Nonlinear. Sci. Numer. Simulat., 73 (2019) 217–228.
[35] G. Zhu, J. Kou, B. Yao, Y. Wu, J. Yao, S. Sun, Thermodynamically consistent modelling of two-phase flows with moving contact line and soluble surfactants, J. Fluid Mech., 879 (2016) 327–359.
[36] H. Liu, H. Ding, A diffuse-interface immersed-boundary method for two-dimensional simulation of flows with moving contact lines on curved substrates, J. Comput. Phys., 294 (2015) 484–502.
[37] P. Yue, Thermodynamically consistent phase-field modelling of contact angle hysteresis, J. Fluid Mech., 899 (2020) A15.
[38] Y. Li, J. Choi, J. Kim, Multi-component Cahn-Hilliard system with different boundary conditions in complex domains, J. Comput. Phys., 323 (2016) 1–16.
[39] J. Yang, J. Kim, A phase-field method for two-phase fluid flow in arbitrary domains, Comput. Math. Appl., 79(6) (2020) 1857–1874.
[40] J. Yang, J. Wang, J. Kim, Energy-stable method for the Cahn–Hilliard equation in arbitrary domains, Int. J. Eng. Sci., 228 (2022) 107489.
[41] T. Young, An essay on the cohesion of fluids, Phil. Trans. R. Soc. Lond., 95 (1805) 65–87.
[42] Y. Li, J. Choi, J. Kim, A phase-field fluid modeling and computation with interfacial profile correction term, Commun. Nonlinear. Sci. Numer. Simulat., 30 (2016) 84–100.
[43] Q. Xia, J. Kim, Y. Li, Modeling and simulation of multi-component immiscible flows based on a modified Cahn–Hilliard equation, Eur. J. Mech. B Fluids, 95 (2022) 194–204.
[44] J. Yang, Wu, J., Tan J., Phase-field modeling and consistent energy-stable simulation of binary creeping flows in contact with solid, Comput. Methods Appl. Mech. Engrg., 414 (2023) 116180.
[45] J. Yang, Z. Tan, J. Wang, J. Kim, Modified diffuse interface fluid model and its consistent energy-stable computation in arbitrary domains, J. Comput. Phys., 488 (2023) 112216.
[46] J. Wu, J. Yang, Z. Tan, Unconditionally energy-stable time-marching methods for the multiphase conservative Allen–Cahn fluid models based on a modified SAV approach, Comput. Methods Appl. Mech. Engrg., 398 (2022) 115291.
[47] J. Yang, J. Kim, A variant of stabilized-scalar auxiliary variable (S-SAV) approach for a mod-

ified phase-field surfactant model, Commun. Comput. Phys., 261 (2021) 107825.
[48] A. Baskaran, Z. Hu, J.S. Lowengrub, C. Wang, S.M. Wise, P. Zhou, Energy stable and efficient finite difference nonlinear multigrid schemes for the modified phase field crystal equation, J. Comput. Phys. 250 (2013) 270–292.
[49] H. G. Lee, J. Kim, Accurate contact angle boundary conditions for the Cahn–Hilliard equations, Comput. Fluids, 44 (2011) 178–186.
[50] J. Kim, An augmented projection method for the incompressible navier-stokes equations in arbitrary domains, Int. J. Compt. Meth., 2 (2005) 201–212.
[51] Q. Xia, J. Kim, B. Xia, Y. Lia, An unconditionally energy stable method for binary incompressible heat conductive fluids based on the phase-field model, Comput. Math. Appl., 123 (2022) 26–39.